Werk

Jahr: 1986
Kollektion: fid.geo
Signatur: 8 Z NAT 2148:60
Digitalisiert: Niedersächsische Staats- und Universitätsbibliothek Göttingen
Werk Id: PPN1015067948_0060
PURL: http://resolver.sub.uni-goettingen.de/purl?PPN1015067948_0060

LOG Id: LOG_0027
LOG Titel: GRF broad-band array analysis of the 1982 Miramichi, New Brunswick earthquake sequence
LOG Typ: article

Übergeordnetes Werk

Werk Id: PPN1015067948
PURL: http://resolver.sub.uni-goettingen.de/purl?PPN1015067948
OPAC: http://opac.sub.uni-goettingen.de/DB=1/PPN?PPN=1015067948

Contact

Niedersächsische Staats- und Universitätsbibliothek Göttingen
Georg-August-Universität Göttingen
Platz der Göttinger Sieben 1
37073 Göttingen
Germany
Email: gdz@sub.uni-goettingen.de

J Geophys (1986) 60:120–128

Journal of Geophysics

Original investigations

GRF broad-band array analysis of the 1982 Miramichi, New Brunswick earthquake sequence*

P.W. Basham[1] **and R. Kind**[2]

[1] Geophysics Division, Geological Survey of Canada, 1 Observatory Cr., Ottawa, Canada K1A OY3
[2] Seismologisches Zentralobservatorium Gräfenberg, Krankenhausstraße 1–3, 8520 Erlangen, Federal Republic of Germany

Abstract. Digital broad-band seismic data from the Gräfenberg array station (GRF) in southern Germany and reflectivity-method theoretical *P*-wave modelling place new constraints on focal depth and mechanism dip of the four principal 1982 Miramichi, New Brunswick, Canada, earthquakes. Relying on previous information for the choice between conjugate dip directions, the m_b 5.7 mainshock is confirmed to have occurred at a depth of 7 km with an average westward dip of about 60°. It was preceded by 0.9 s by a precursory rupture of about m_b 5.2. The first large aftershock (m_b 5.1) occurred at a depth of 6 km and average dip 55° in the region of the lower portion of the mainshock rupture. The largest aftershock (m_b 5.4), confined to the conjugate, east-dipping plane, ruptured from a depth of 6 km with an average dip of 50°. The third large aftershock (m_b 5.0) occurred in the shallow region of the mainshock with a depth of about 3.5 km and 50° dip. Broad-band array data prove very useful for even the smallest events in this sequence, and waveform modelling of such data provides close constraints on some source parameters. In the case of the Miramichi earthquakes there is good resolution on depth (±1 km) and dip (±10°), but little resolution on rake and strike.

Key words: New Brunswick, Canada, earthquakes – Thrust faulting – Gräfenberg array – Reflectivity method – Theoretical seismograms

Introduction

The m_b 5.7 mainshock that occurred on 9 January 1982 at 12:53 in the Miramichi region of north-central New Brunswick, Canada (Fig. 1), was the largest historical earthquake in New Brunswick and the largest earthquake in eastern Canada since the Cornwall-Massena earthquake of 1944. The mainshock was followed by an extensive aftershock sequence with principal aftershocks on 9 January at 16:36 (m_b 5.1), 11 January at 21:41 (m_b 5.4) and 31 March at 21:02 (m_b 5.0). Wetmiller et al. (1984) have presented an extensive analysis of the earthquake sequence, based mainly on field recordings of aftershocks. Choy et al. (1983) have determined the source characteristics of the mainshock from recordings of the Global Digital Seismograph Network. Basham and Adams (1984) have presented some speculations on the types of fault systems in the upper crust that may be responsible for the earthquakes in the presence of an east-west horizontal stress regime. Mueller and Cranswick (1985), Saikia and Herrmann (1985) and Cranswick et al. (1985) have presented analyses of some of the smaller aftershocks in the Miramichi sequence.

We will begin this analysis from the basis of the conceptual model of the four principal shocks (Fig. 2) developed by Wetmiller et al. and discussed further by Basham and Adams. Briefly, the hypothesis is as follows. The mainshock of m_b 5.7 was a thrust mechanism with rupture up-dip on a west-dipping plane from a depth of about 7 km. This was followed 3.5 h later by the m_b 5.1 aftershock, located somewhere on or near the lower portion of the mainshock rupture surface. The m_b 5.4 aftershock ruptured, probably up-dip, the conjugate east-dipping plane 2.5 days later. And finally, 2.5 months later, the m_b 5.0 aftershock occurred somewhere on or near the upper portion of the mainshock rupture surface.

As indicated by Wetmiller et al. (1984), not all aspects of this hypothesis are yet proven by available data. The general characteristics of the mainshock are not in doubt and there is convincing evidence that its rupture surface steepens as it approaches the surface. There is also a suggestion (Choy et al., 1983) that the main rupture was a double event with the crack growth momentarily interrupted by a fracture barrier. There is no good independent evidence for the location of the m_b 5.1 aftershock; its speculated location in the region of the lower portion of the main rupture is a convenience, given the shallow occurrence of the m_b 5.0 aftershock. The principal evidence for a conjugate rupture by the m_b 5.4 event came from the aftershock distribution in the early days of the field monitoring (following this event) which showed most of the smaller aftershocks scattered about this east-dipping plane. The location of the m_b 5.0 aftershock is inferred from a concentration of smaller aftershocks in the shallow, northeastern portion of the active zone established by field observations for a few days following this event.

It is this hypothesis of the characteristics of the four principal Miramichi earthquakes that we wish to assess using the broad-band Gräfenberg (GRF) array data and theoretical waveform modelling. In particular, we wish to establish the constraints that can be put on the focal depths and mechanism orientations of these closely spaced, moderate magnitude earthquakes using broad-band data from a teleseismic array and associated modelling.

* Geological Survey of Canada Contribution Number 19386

Offprint requests to: R. Kind

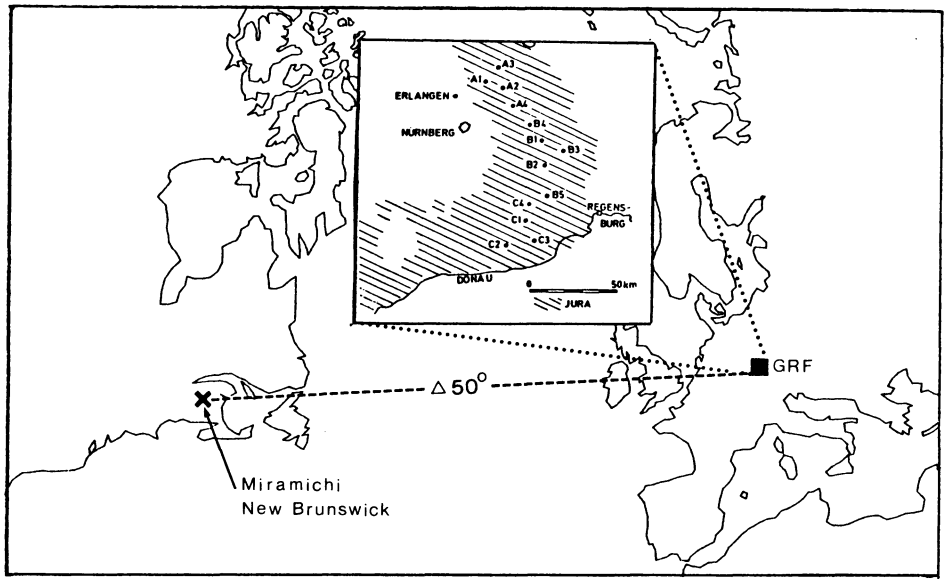

Fig. 1. Location map showing the epicentre of the Miramichi, New Brunswick, earthquakes in eastern Canada and the GRF array in southern Germany (epicentral distance 50°). The configuration of the GRF array is shown in the *inset*

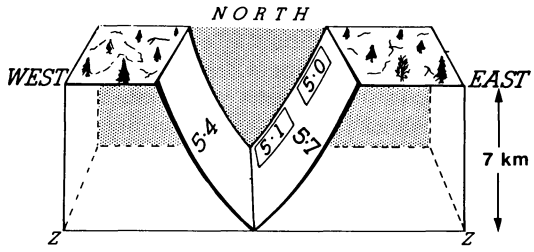

Fig. 2. Perspective view of the suggested orientations of the Miramichi mainshock (m_b 5.7) and its three main aftershocks. (After Basham and Adams, 1984.)

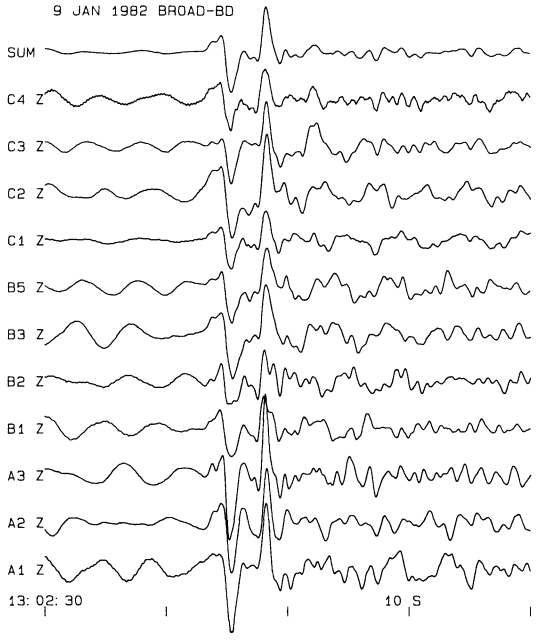

Fig. 3. Broad-band velocity recordings from the 11 available channels of the GRF array for the Miramichi mainshock *P* wave. The SUM trace at the *top* is produced by delay and sum of the 11 channels for an azimuth of 294° and a slowness of 7.3 s/deg. Tick marks on the time axis are every 10 s

The GRF array and data processing

The 13-element broad-band GRF array in northern Bavaria, FRG, has an aperture of about 40×100 km^2 (see inset in Fig. 1). The 13 elements have vertical, and 3 have horizontal, broad-band Wielandt seismometers with a flat velocity response between 20 s and 5 Hz. The dynamic range of the data acquisition system is 132 dB and the resolution is 66 dB. A complete description of the array is given by Harjes and Seidl (1978). Data from the array can be studied using simulations of different seismograph responses (broad-band displacement, SRO, WWSSN, LRSM, etc.) in order to enhance particular characteristics of waveforms (Seidl, 1980; Seidl and Stammler, 1984).

GRF data has been successfully applied in studies of: regional body waves and source properties (Kind, 1979a, 1981; Räkers and Müller, 1982; Seidl and Berckhemer, 1982; Zonno and Kind, 1984; Faber and Bonjer, 1985; Barbano et al., 1985), regional surface waves (Brüstle and Müller, 1983; Hanka, 1982) and teleseismic body waves (Upadhyay and Duda, 1980; Kind and Seidl, 1982; Brüstle, 1985; Engdahl and Kind, 1986). Many of these have been single array-station (GRF) studies of particular earthquakes and earthquake sequences.

GRF recordings of the Miramichi events

Figure 3 shows all available GRF vertical broad-band velocity recordings of the Miramichi mainshock. The SUM trace shown at the top was produced by fitting a plane-wave arrival to picks of the first major through on the 11 channels. Considerable variations in amplitude, but not in general pulse characteristics, are seen across the array. Sub-array A generally records the largest amplitudes for this event; sub-arrays B and C are more variable in amplitude across the sub-arrays. Station B2 shows signal characteristics that differ most from "average" signal characteristics shown in the SUM trace. Nevertheless, the important characteristics seen in the SUM can be seen in each individual channel, confirming that these are produced by near-source effects and not by near-station effects.

Therefore, the Miramichi mainshock broad-band velocity recorded at GRF can be characterized by two large velo-

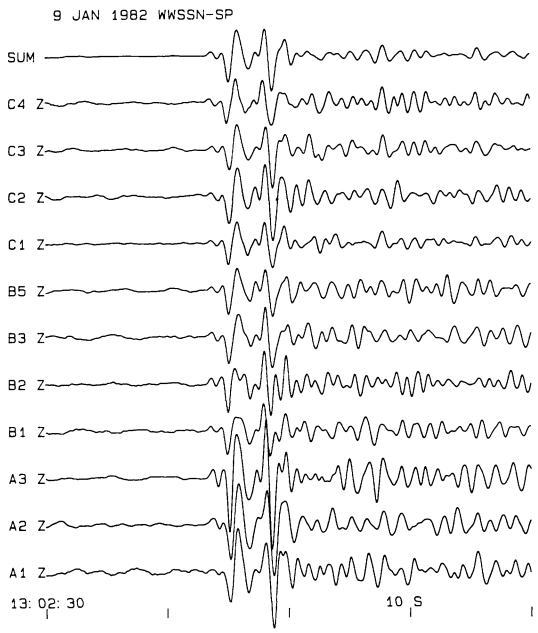

Fig. 4. As in Fig. 3 with a WWSSN-SP filter

city pulses of equal amplitude and opposite sign separated by about 3 s. Each of these pulses is preceded by a precursory pulse producing a flattening in the onsets of the main pulses. The second main pulse has been interpreted by Choy et al. (1983) as *sP*. (Choy et al. used the A3 record in their body-wave modelling.) They also interpreted the precursor as a momentary stopping of crack growth by a fracture barrier, which then failed producing the main rupture event. Both of these interpretations will be treated below as part of the theoretical modelling.

The simulated WWSSN-SP response to the mainshock is shown in Fig. 4. All important characteristics of the *P* wave are preserved with this narrower band filtering, indicating that the dominant energy falls within the WWSSN-SP passband. The two main pulses are very clear and the precursors to the main pulses are somewhat enhanced over what can be observed in the broad-band recordings.

SUM recordings of broad-band velocity and WWSSN-SP for the mainshock and three aftershocks are shown in Figs. 5 and 6, respectively. The 11 January aftershock, smaller than the mainshock by 0.3 m_b units, has a lower signal-to-noise ratio on the broad-band SUM (Fig. 5). Nevertheless, it is clear that the *P*-wave group for this event differs significantly from that of the mainshock. It is a single velocity wavelet followed by higher frequency energy superimposed on a broader pulse. The broader secondary pulse may be source-generated, but may also be due to a partially coherent microseism cycle that is retained in the SUM. With the WWSSN-SP filter (Fig. 6), the secondary energy after the first pulse appears as ringing with a period of about 0.9 s. Explaining the difference between this aftershock, believed to be the principal rupture on the conjugate fault plane, and the mainshock is one of the principal tasks of the modelling described below.

The two smaller aftershocks (9 January, m_b 5.1, and 31 March, m_b 5.0) have poor long-period signal-to-noise ratio in the broad-band SUM (Fig. 5), although the SUM has significantly improved the signal-to-noise ratio over that available on a single channel. This illustrates the advantage of a broad-band array over a single station in studies of moderate magnitude earthquakes. The differences among the four events are seen most clearly with the WWSSN-SP filter. The signals in Fig. 6 are aligned on the first major trough, which is a common feature of the four *P* waves. The amplitudes of the three aftershocks relative to the mainshock have been scaled by the factors shown in the figure. The 9 January aftershock has a second strong velocity pulse, but it precedes the second pulse of the mainshock (the trough of which is shown by line segments) by about 0.8 s. The 31 March aftershock has no strong secondary pulse and little energy above the background noise level in this time period. These two aftershocks are speculated to be on the lower and upper portions, respectively, of the mainshock fracture surface. We also address this question with modelling below.

Theoretical seismograms

The reflectivity method for computing theoretical seismograms was developed by Fuchs (1968) and Fuchs and Müller (1971). Kind (1978, 1979b) developed a version of the method for the computation of complete earthquake seismograms, and extended the method to allow the computation of complete body waves for different source and re-

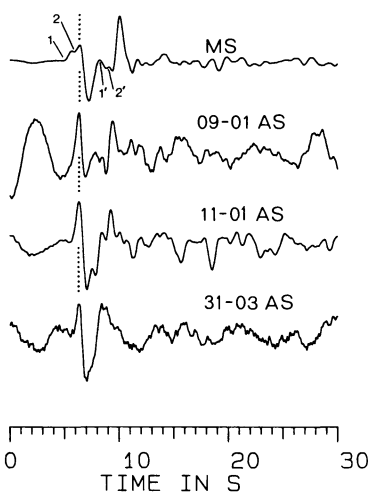

Fig. 5. Broad-band velocity SUM seismograms for the Miramichi mainshock (MS) and three aftershocks (AS). The signals have been aligned on the first major peak. The principal phases identified for the mainshock are: 1, *P* wave of precursor; 2, main *P* wave; 1′, possible *sP* of precursor; 2′, *sP*

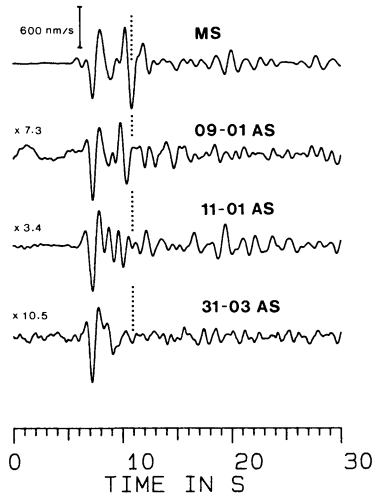

Fig. 6. WWSSN-SP SUM seismograms for the mainshock (MS) and three aftershocks (AS). The signals have been aligned on the first major trough. Vertical line segments are shown at the time of the second major trough of the mainshock. Signals are plotted with equal maximum amplitudes. *Vertical bar* above first record shows amplitue scale. Plot scaling factors are shown for the subsequent events

ceiver structures (Kind, 1985). The latter version of the method is used here to model the Miramichi earthquake *P* waves.

The source is a dislocation double-couple point source whose orientation is defined by the three angles, strike (ϕ), dip (δ) and slip (or rake, λ). The source time function used is that of Brüstle and Müller (1983) in which the moment function describes a smooth increase to the final moment during the rise time T. The corresponding far-field displacement, the only function actually employed in the modelling described here, is a simple single-sided pulse with duration T. Brüstle and Müller have emphasized that in this representation T has nothing to do with the rise time of the dislocation on the rupture surface. Neither are we concerned with the absolute amplitude of the pulse, the final moment, as we do not attempt to model moment estimates for these earthquakes. In the principal modelling we will vary the three source orientation angles and focal depth to attempt to match observed signals.

The rise time, T, is varied in the initial modelling until a reasonable fit of the pulse width is achieved in a long-period component (e. g. broad-band displacement). Short-period seismograms are then checked to see if this value of T produces appropriate higher frequency energy. If not, the value of T is decreased, i. e. the equivalent corner frequency of the source spectrum is increased, until a reasonable short-period match is achieved. This does not give a high degree of resolution on T, but appropriate values were found to be 1.5 s for the mainshock and 1.0 s for the three aftershocks. These values have been used for the theoretical seismograms described below.

The Miramichi earthquakes occurred in a massive granite pluton. The source crust is modelled with a simple single-layer crust 36 km thick with a *P*-wave velocity of 6.2 km/s over an 8.2-km/s upper mantle. *S*-wave velocities are scaled from the *P*-wave velocities by dividing by the square root of 3. The artificial interface between the source region and the mantle (and between the receiver region and the mantle) required by the method (see Kind, 1985) is at a depth of 100 km. The Jeffreys-Bullen mantle model is used.

The receiver crust is a simplified model of the crust under GRF. It consists of a 30-km-thick layer with a *P*-wave velocity of 6 km/s over an 8-km/s upper mantle. The GRF array is underlain by Mesozoic sediments with a *P*-wave velocity of about 3.5 km/s whose thickness varies from about 300 m at stations in the south to about 2 km at stations in the north. The differences in sediment thickness and structure of the crust produce the different signal characteristics seen across the array (Figs. 3 and 4). For comparison with theoretical seismograms we will use the SUM signals, which in a gross manner average out the crustal differences across the array. Once a reasonable match to the mainshock signal was obtained with no surficial sediments in the GRF crust, experiments were undertaken to assess the influence on the theoretical seismograms of sediment thicknesses up to 2 km. It was found that up to 500 m of sediments produced no discernable difference in the theoretical seismograms: 1 km of sediments introduced additional high-frequency energy into the signals; and 2 km of sediments tended to attenuate the high-frequency energy. The 1-km sedimentary layer, which is a reasonable average for the sediment thickness across the array, produced the greatest improvement in the match with observed broad-band and WWSSN-SP filtered SUM signals. Therefore, 1 km of 3.5-km/s sediments was added to the final GRF receiver crust.

Clearly, there is a trade-off between the energy content as a function of frequency introduced into the theoretical seismograms by the assumed source spectrum and by the model for the GRF crust (as well as by the attenuation over the whole travel path). The overall model is therefore not unique and we should not expect to model minor observed signal characteristics and attribute them to the source.

The method used here cannot give diagnostic information on the actual plane of rupture. For thrust faults, conjugate east- and west-dipping mechanisms have identical radiation patterns, and therefore produce identical theoretical seismograms, for complementary values of dip angle. The modelling cannot distinguish between, for example, a 60° east-dipping and a 30° west-dipping pure thrust for any values of strike. Therefore, the choice between the conjugate east- or west-dipping ruptures must be constrained by other information, and we will rely mainly on the earlier results of Wetmiller et al. (1984) and Choy et al. (1983) in choosing between conjugate mechanisms.

Results and discussion

Mainshock

The general characteristics of the mechanism of the mainshock established by Wetmiller et al. (1984) and Choy et al. (1983) were a west-dipping thrust with approximately north-south strike. The starting model for the theoretical seismograms was therefore a pure thrust ($\lambda = 90°$) with south strike ($\phi = 180°$) and dip of 45° to the west ($\delta = 45°$). In addition to focal depth (h) governing the delay times of the depth phases pP and sP, initial modelling indicated that the relative amplitudes of pP and sP were sensitive to the dip angle and, once sP is established as the dominant depth phase, its amplitude relative to P is sensitive to rake and strike. It is apparent, however (Figs. 3 and 4), that the precursor is causing some destructive interference with the two main velocity pulses of the mainshock. This suggests that unless we attempt to account for the influence of the precursor, we cannot rely too heavily on the relative amplitudes of P and the depth phase. Therefore, again using a preliminary result for the mainshock, we undertook experiments to simulate the precursor.

If we accept the assumption that the precursor is the initial rupture momentarily stopped by a barrier, it will have a signal character similar to the main rupture but reduced in amplitude and advanced in time. This was simulated by taking the theoretical seismogram of the mainshock and adding to it the same seismogram reduced in amplitude and advanced in time, with a number of trial amplitude reductions and time shifts. This implicitly assumes that the precursor and main rupture occurred at the same hypocentre, which is physically unrealistic, but has no influence on producing a *P*-wave signal appropriate for the precursor. The results suggest an amplitude of 0.3 and a time advance of 0.9 s for the precursor. The amplitude ratio indicates that the precursory rupture is about 0.5 m_b units smaller than the main rupture. This simulated precursor has been added to all of the theoretical mainshock seismograms discussed below.

We present the modelling results (Fig. 7) with three of

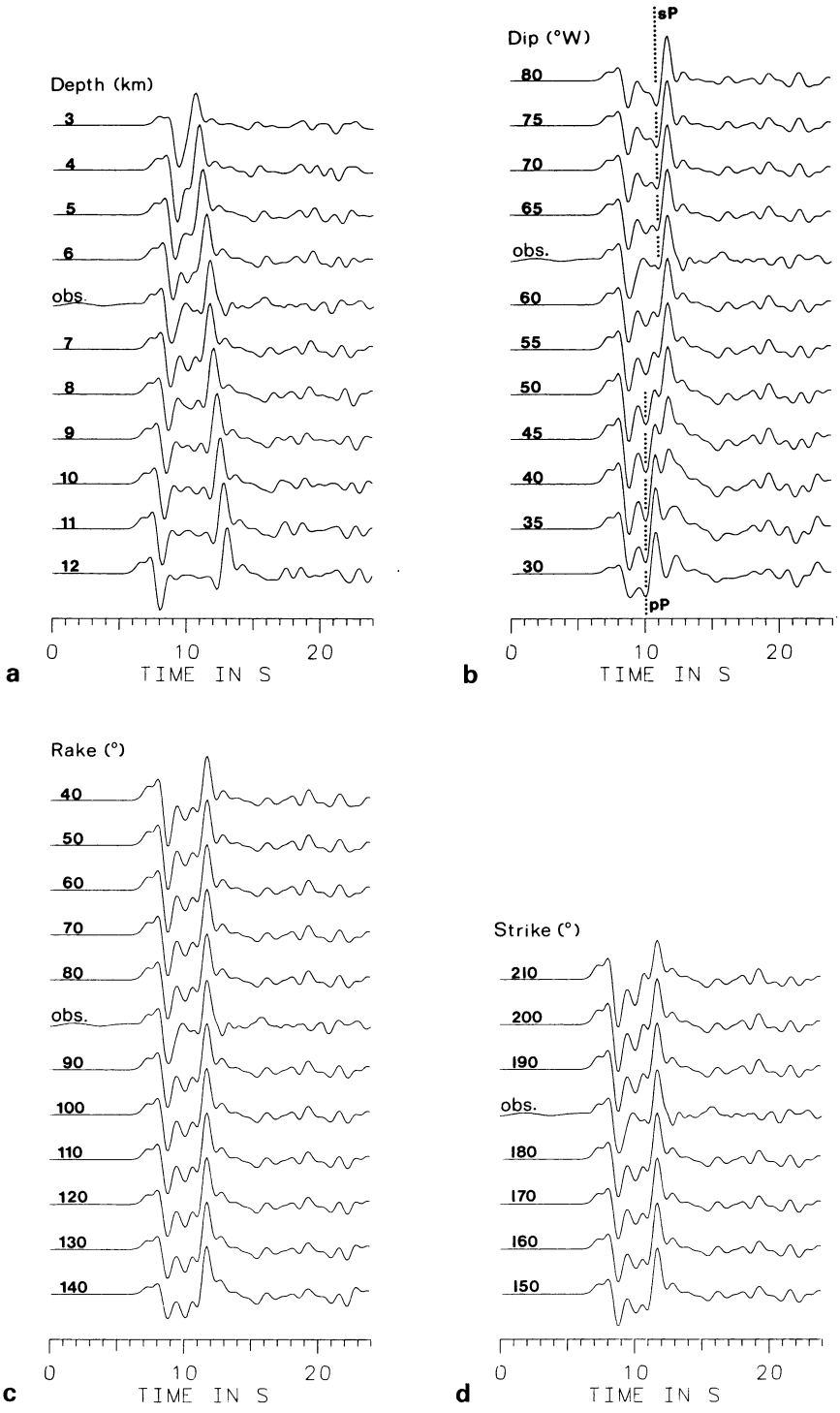

Fig. 7a–d. Theoretical broad-band velocity seismograms for the mainshock, including the precursor with amplitude 0.3 of the main rupture and time advance of 0.9 s. Adopted parameters are $h=7$ km, $\delta=60°$ west, $\lambda=90°$ and $\phi=180°$. The theoretical seismograms are shown with variable **a** depth, **b** dip, **c** rake and **d** strike with the other three parameters fixed at their adopted values. The observed seismogram (obs.) is superimposed above the theoretical seismogram with the appropriate value of the varying parameter

the four parameters (h, δ, λ, ϕ) fixed at their final values with the other varying over a fairly wide range to show its influence. Note that in each of the theoretical seismograms a precursor has been added as described above, assuming that in each model variation the precursor and the main rupture have the same model parameters.

In Fig. 7a, the effect of focal depth on the arrival time of *sP* is obvious. The time difference between the positive *P* and *sP* peaks in the observed seismogram matches exactly the time difference in the theoretical seismogram for a depth of 7 km. This time difference is about 0.5 s too small for $h=6$ and 0.5 s too large for $h=8$. Therefore, we suggest the resolution of focal depth is better than 1 km. Although Wetmiller et al. (1984) estimated a mainshock depth of 7 km based on aftershock distribution and surface-wave analysis, Choy et al. (1983) established a depth of 9 km. We believe that Choy et al. have over-estimated the depth by measuring the time interval from the onset of the precursor (rather than the main pulse) to the onset of the main depth phase pulse; i. e. their *sP-P* and *pP-P* intervals are about 1 s too large. It is possible in these data (see mainshock in Fig. 5) to also identify what may be the precursor

to *sP*, which makes the correspondence between the principal *P* and *sP* pulses very clear.

Figure 7b shows that the amplitudes of *pP* and *sP* are significantly affected by the dip angle. The amplitudes of the two depth phases are approximately equal for $\delta = 45°$; *pP* dies out for steeper dips, *sP* for shallower dips. The simple double-pulse nature of the observed seismogram can best be matched by *sP* for dip in the range 50°–70°. For dips less than 50°, the waveform match deteriorates because of the emergence of *pP*; for dips greater than 70°, the theoretical *sP* pulse is too strong relative to *P*. A single *pP* depth phase would be produced with the appropriate time delay with greater focal depth and shallower dip, but the theoretical seismograms show that this would be near a node for *P*. We have adopted $\delta = 60°$, and suggest a resolution of about 10° on this angle.

From composite *P*-nodal solutions of small aftershocks, Wetmiller et al. showed that both the west- and east-dipping rupture surfaces steepen as they approach the surface. For the west-dipping surface the dip is about 50° at depth and about 77° near the surface. Choy et al. (1983) estimated a dip of 65° for the mainshock from analysis of relative amplitudes and polarities of direct *P* and surface reflections. Wetmiller et al. (1984) estimated a dip of 47°–53° from *P* first motions. For an up-dip rupture, the mainshock first motions should be representative of the (smaller) dip at depth. The theoretical seismograms produced here with a point-source model of the rupture can be expected (like the Choy et al. analysis) to be indicative of only the average dip of the rupture surface.

Figure 7c shows that the theoretical seismograms are not very sensitive to quite large variations in the rake angle. For λ near 140°, the relative amplitude of *sP* appears too large. For λ between 40° and 100°, the match with the observed seismogram is considered equally good. We have adopted $\lambda = 90°$ (i. e. pure thrust) but do not claim to have much resolution on this angle. [Wetmiller et al. (1984) estimated a rake of 120°; Choy et al. (1983), a rake of 65°.] Figure 7d shows that the theoretical seismograms are not very sensitive to strike. The relative amplitude of *sP* is too large for strikes near 150° and too small near 210°. The match is considered equally good for strikes in the range 170°–200°. Both Wetmiller et al. and Choy et al. found values of $\phi = 195°$. We have adopted a value of $\phi = 180°$ (i. e. north-south).

The final results for the mainshock are shown in Fig. 8 for the broad-band, WWSSN-SP and displacement passbands. The final match achieved with the broad-band and WWSSN-SP filters is considered very good. It was found during the experiments with the GRF sedimentary layer described earlier that the match of the theoretical and observed signals with the displacement passband could be improved from that shown if we included 2 km of GRF sediments, i. e. removed some of the high-frequency energy; but this worsened the match in the broad-band and WWSSN-SP passbands. This is an indication of the non-uniqueness of the overall model (source, attenuation and GRF crust) in introducing frequency content into the theoretical seismograms.

11 January aftershock

The principal difference from the mainshock seen in the observed seismograms of the 11 January aftershock is a

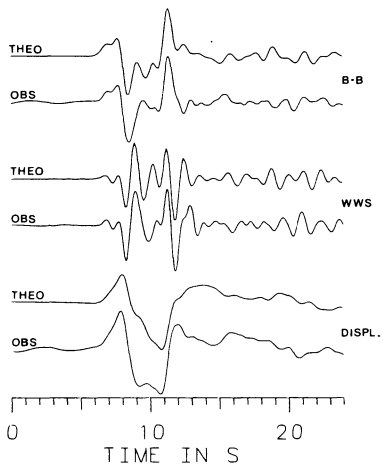

Fig. 8. Comparison of final mainshock theoretical seismograms (Theo.) with observed signals (Obs.) in the broad-band, WWSSN-SP and displacement passbands

"ringing", or interference pattern, following the main *P* pulse, seen best in the WWSSN-SP seismograms (Fig. 6), and the absence of a clear depth phase. As indicated above, the theoretical seismograms cannot distinguish between complementary values of east and west dip angles. Therefore, we restrict the modelling to eastward dip on the basis of the convincing east-dipping trend of small aftershocks shown by Wetmiller et al. (1984). The goal of the modelling is to find appropriate values of focal depth and average dip angle for this aftershock.

Choy et al. studied the seismogram at one station (ZOBO) for this event, at an azimuth that showed a depth phase interpreted as *pP* indicating a focal depth of 6 km. Therefore, the starting model for the theoretical seismograms was an east-dipping pure thrust ($\phi = 0°$, $\lambda = 90°$) at a depth of 6 km. The theoretical seismograms are compared with the observed signals in Fig. 9. Figure 9a shows an effect of dip on the theoretical seismograms opposite to that seen for the mainshock in Fig. 7b. For the east-dipping rupture, *pP* is strong for large values of dip and *sP* strong for small values of dip. The first cycle of the observed signal is matched well by the theoretical seismograms with dip in the range 30°–50°. The second part of the signal is matched best for dip in the range 45°–55°, where the interference between *pP* and *sP* seems to be the strongest. We have adopted a dip of 50° and suggest a resolution of about 10°.

Figure 9b, computed for a dip of 50°, shows the effect of focal depth and confirms that a depth of 6 km is appropriate for this aftershock. However, with the lack of a clear depth phase among the ringing signal, there is no clear time delay on which to base a resolution on depth. Comparison of Figs. 9a and 9b shows that the characteristics of *pP-sP* interference change quite appreciably over small ranges of both dip and focal depth. Therefore, different combinations of the two could produce an equivalent match with the observed signals. As was found for the mainshock, the theoretical seismograms for this aftershock provide little resolution on rake or strike, and we have retained pure thrust with north strike.

This ringing, or interference phenomenon, now attributed to interference of *pP* and *sP* which have similar amplitudes for this dip, was seen most clearly in the WWSSN-SP

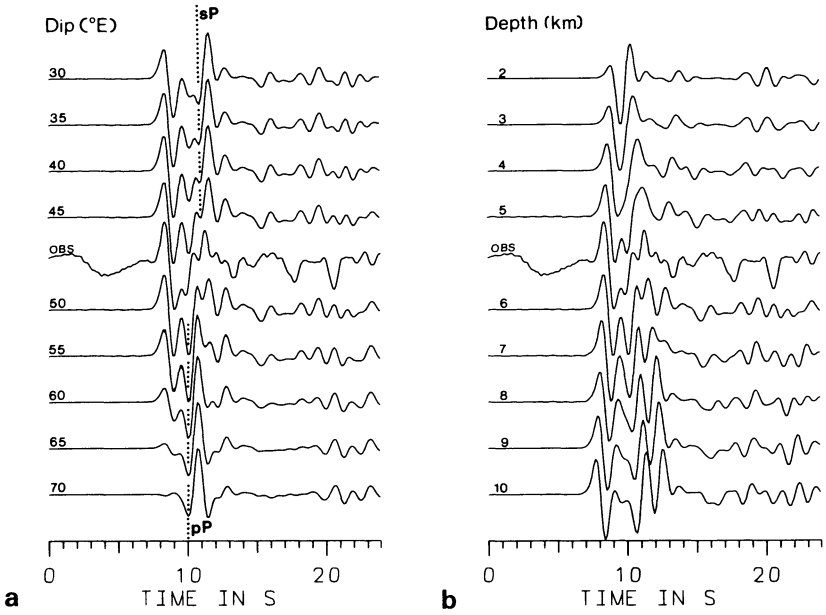

Fig. 9a and b. Theoretical broad-band velocity seismograms for the 11 January aftershock: **a** with variable eastward dip for a depth of 6 km; **b** with variable depth for an eastward dip of 50°. The observed seismogram (obs.) is superimposed above the theoretical for dip = 50° and depth = 6 km

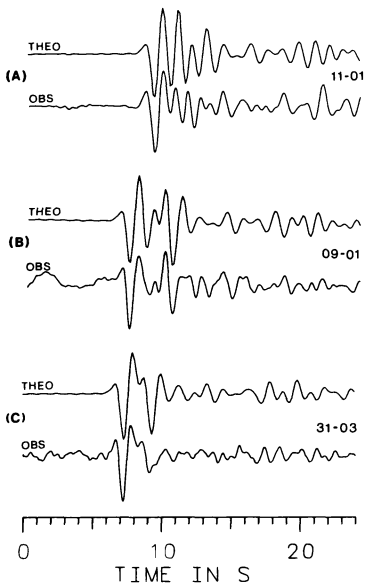

Fig. 10a–c. Theoretical (*upper*) and observed (*lower*) WWSSN-SP filtered seismograms for the 11 January, 9 January and 31 March aftersthocks. **a** The 11 January theoretical seismogram is computed for a focal depth of 6 km and eastward dip 50°, **b** the 9 January seismogram for depth 6 km and westward dip of 55° and **c** the 31 March seismogram for depth 3.5 km and westward dip 50°

filtered signal (Fig. 6). The WWSSN-SP filtered theoretical seismogram is compared with the observed signal in Fig. 10a. The match is reasonable, but the ringing phenomenon is too strong in the theoretical seismogram. In retrospect, this difference is apparent in the broad-band seismograms in Figs. 9a and b. The observed seismogram seems to have a low-amplitude ringing superimposed on a long-period signal, which may be a half cycle of the long-period noise seen in front of the *P* onset to be quite strong. In any case, with the model variations that we have tested, we cannot improve on this match of the short-period ringing phenomenon.

9 January and 31 March aftershocks

The general character of the signal of the 9 January aftershock is very similar to that of the mainshock, i. e. two simple velocity pulses representative of direct *P* and a depth phase (e. g. Fig. 6). This suggests a very similary mechanism, with a small difference in focal depth. The 31 March aftershock exhibits no clear depth phase. However, the spatial clustering of small aftershocks in the shallow region of the west-dipping rupture following this event, shown by Wetmiller et al., is sufficient evidence to also confine this aftershock to the shallow region of the west-dipping rupture. The modelling for these two events, therefore, becomes an attempt to independently determine focal depth and source orientation with west dip.

As was illustrated for the mainshock described above, the theoretical seismograms are not sensitive to quite large variations in rake and strike. Therefore, these two aftershocks are also assumed to be pure thrust on south-striking, west-dipping faults, and the model variations are made only for dip and focal depth. Dip controls the relative amplitudes of *P* and *sP* and depth the delay time of *sP*. Iterations of these two model parameters have produced the theoretical seismograms that are compared with the WWSSN-SP filtered signals in Fig. 10b and c. The agreement achieved for the 9 January aftershock with a dip of 55° and focal depth of 6 km is quite good. The resolution of dip is about 10° and of depth less than 1 km. Although in this study we cannot provide new information on the absolute locations of these aftershocks, this result confirms the speculation by Wetmiller et al. that the 9 January aftershock was located near the lower portion of the mainshock rupture surface.

The result for the 31 March aftershock with a depth of 3.5 km and dip of 50° is also quite good. The character of the theoretical seismograms following the first full cycle is very sensitive to small changes in depth and dip. And although there is a trade-off between these two parameters over small ranges, they cannot be significantly different from the adopted ones. The main difference between the two signals is the somewhat stronger negative depth phase

pulse in the theoretical seismogram. Therefore, even for this, the shallowest of the aftershocks, we suggest a depth resolution of less than 1 km and dip resolution of about 10°. The result is in good agreement with the results from smaller aftershocks shown in Fig. 15 of Wetmiller et al. (1984): the hypocentres are clustered at depths less than 3.5 km and their composite mechanism has a dip of 49°.

Conclusions

This analysis of the four principal Miramichi, New Brunswick, earthquakes using GRF broad-band data and reflectivity-method theoretical seismograms has produced results that are consistent with the conceptual model for these earthquakes developed by Wetmiller et al. (1984) and Choy et al. (1983). In a number of aspects the analysis has strengthened the previous suggestions. The prior knowledge of the thrust mechanisms due to east-west compressive stress has enabled us to converge on acceptable theoretical seismograms without sampling the entire parameter space of the four parameters depth, dip, rake and strike. Prior information on dip direction enabled estimates of focal depth and average dip angle from theoretical seismograms, which otherwise would be ambiguous with respect to complementary dip angles for opposite dip directions.

The general characteristics of the mainshock were not previously in doubt. The theoretical seismograms match the GRF recordings best for a focal depth of 7 km and average westward dip of 60°. Pure thrust with north-south strike has been adopted, but this single-station analysis provides little constraint on the source parameters (for all four events). In fact, the lack of influence of strike and rake (within reasonable bounds) on the theoretical seismograms gives us more confidence in the determination of average dip angles, to which the waveforms are quite sensitive. The suggestion by Choy et al. that the initial rupture was momentarily stopped by a fracture barrier is supported by modelling which indicates that a precursory rupture about 0.5 m_b units smaller preceded the main rupture by about 0.9 s.

The 9 January aftershock, the previously most uncertain of the four, is confirmed to have occurred in the region of the lower portion of the mainshock rupture. It has a well-constrained focal depth of 6 km and an average westward dip of about 55°. The 11 January aftershock, confined by other information to the east-dipping rupture surface, originated at a depth of about 6 km and had an average dip of about 50°. The 31 March aftershock, shown by previous work to be in the shallow region of the mainshock rupture, is matched best with a focal depth of about 3.5 km and westward dip of 50°.

This analysis, based on the data from a broad-band array station which recorded these four earthquakes with good signal-to-noise ratio, particularly in the short-period (WWSSN-SP) passband, has produced good focal depth (± 1 km) and average dip ($\pm 10°$) resolution on moderate-magnitude shallow earthquakes. The availability of array data, rather than single-sensor data, has enabled improvements to signal-to-noise ratio for marginal signals and has improved confidence that observed signal characteristics are source-related and not due to path effects local to one or more stations. The results suggest that more information, particularly on the strike and rake angles of the four events, would be gained using this simple modelling and other types of analysis on high-quality, teleseismic data at other azimuths.

Acknowledgements. This work was performed while the first author was a guest scientist at the Seismologisches Zentralobservatorium Gräfenberg in Erlangen, and he is grateful for the courtesy and assistance of the Observatory staff. We thank H. Hanka for computing assistance, and John Adams, George Choy, Sonja Faber, Henry Hasegawa, Bob North, Deiter Seidl and Max Wyss for comments and discussion. The GRF-array project is supported by the Deutsche Forschungsgemeinschaft and the Bundesanstalt für Geowissenschaften und Rohstoffe.

References

Barbano, M.S., Kind, R., Zonno, G.: Focal parameters of some Fruili earthquakes (1976–1979) using complete theoretical seismograms. J. Geophys. **58**, 175–182, 1985

Basham, P.W., Adams, J.: The Miramichi, New Brunswick, earthquakes: near-surface thrust faulting in the northern Appalachians. Geoscience Canada **11**, 115–121, 1984

Brüstle, W.: Der Bruchvorgang im Erdbebenherd – Untersuchung ausgewählter Erdbeben mit beobachteten und synthetischen Seismogrammen. Berichte des Instituts für Meteorologie und Geophysik der Universität Frankfurt/Main, Nr. 63, 1–317, 1985

Brüstle, W., Müller, G.: Moment and duration of shallow earthquakes from Love-wave modelling for regional distances. Phys. Earth Planet. Inter. **32**, 312–324, 1983

Choy, G.L., Boatwright, J., Dewey, J.W., Sipkin, S.A.: A teleseismic analysis of the New Brunswick earthquake of January 9, 1982. J. Geophys. Res. **88**, 2199–2212, 1983

Cranswick, E., Wetmiller, R., Boatwright, J.: High-frequency observations and source parameters of microearthquakes recorded at hardrock sites. Bull. Seismol. Soc. Am. **75**, 1535–1567, 1985

Engdahl, E.R., Kind, R.: Interpretation of broadband seismograms from central Aleutian earthquakes. Ann. Geophys. **4**, B, 3, 233–240, 1986

Faber, S., Bonjer, K.-P.: Phase recognition and interpretation at regional distances from the Liege event of November 8, 1983. In: Seismic activity in western Europe; P. Melchior, ed.: pp. 249–262, D. Reidel Publishing 1985

Fuchs, K.: The reflection of spherical waves from transition zones with arbitrary depth-dependent elastic moduli and density. J. Phys. Earth **16** (Special Issue), 27–41, 1968

Fuchs, K., Müller, G.: Computation of synthetic seismograms with the reflectivity method and comparison with observations. Geophys. J.R. Astron. Soc. **23**, 417–433, 1971

Hanka, W.: Analysis of broad-band Rayleigh waves: a possibility for seismic discrimination. J. Geophys. **51**, 165–179, 1982

Harjes, H.-P., Seidl, D.: Digital recording and analysis of broadband seismic data at the Gräfenberg (GRF)-array. J. Geophys. **44**, 511–523, 1978

Kind, R.: The reflectivity method for a buried source. J. Geophys. **44**, 603–612, 1978

Kind, R.: Observations of *sPn* from Swabian Alb earthquakes at the GRF array. J. Geophys. **45**, 337–340, 1979a

Kind, R.: Extensions of the reflectivity method. J. Geophys. **45**, 373–380, 1979b

Kind, R.: Length of the rupture from the Swabian Alb event on 3 September 1978 derived from the *Pn* duration at GRF. Geol. Jahrb., 13–25, Hannover, 1981

Kind, R.: The reflectivity method for different source and receiver structures and comparison with GRF data. J. Geophys. **58**, 146–152, 1985

Kind, R., Seidl, D.: Analysis of broadband seismograms from the Chile-Peru area. Bull. Seismol. Soc. Am. **72**, 2131–2145, 1982

Mueller, C.S., Cranswick, E.: Source parameters of locally recorded aftershocks of the 9 January 1982 Miramichi, New

Brunswick, earthquake. Bull. Seismol. Soc. Am. **75**, 337–360, 1985

Räkers, E., Müller, G.: The Romanian earthquake of March 4, 1977: III Improved focal model and moment determination. J. Geophys. **50**, 143–150, 1982

Saikia, C.K., Herrmann, R.B.: Applications of waveform modelling to determine focal mechanisms of four 1982 Miramichi aftershocks. Bull Seismol. Soc. Am. **75**, 1021–1040, 1985

Seidl, D.: The simulation problem for broad-band seismograms. J. Geophys. **48**, 84–93, 1980

Seidl, D., Berckhemer, H.: Determination of source moment and radiated seismic energy from broadband recordings. Phys. Earth Planet. Inter. **30**, 209–213, 1982

Seidl, D., Stammler, W.: Restoration of broad-band seismograms (Part I), J. Geophys. **54**, 114–122, 1984

Upadhyay, S.K., Duda, S.J.: Source parameters of earthquakes from the Himalayan region. J. Geophys. **48**, 67–79, 1980

Wetmiller, R.J., Adams, J., Anglin, F.M., Hasegawa, H.S., Stevens, A.E.: Aftershock sequences of the 1982 Miramichi, New Brunswick, earthquakes. Bull. Seismol. Soc. Am. **74**, 621–653, 1984

Zonno, G., Kind, R.: Depth determination of North Italian earthquakes using Graefenberg data. Bull. Seismol. Soc. Am. **74**, 1645–1659, 1984

Received May 6, 1986; revised version July 20, 1986
Accepted August 4, 1986